Copyright © 1982, by the author(s).
All rights reserved.

Permission to make digital or hard copies of all or part of this work for personal or classroom use is granted without fee provided that copies are not made or distributed for profit or commercial advantage and that copies bear this notice and the full citation on the first page. To copy otherwise, to republish, to post on servers or to redistribute to lists, requires prior specific permission.

MEGAVOLT ARSENIC IMPLANTATION INTO SILICON

by

P.F. Byrne

Memorandum No. UCB/ERL M82/62

12 August 1982

ELECTRONICS RESEARCH LABORATORY
College of Engineering
University of California, Berkeley
94720

P.F. Byrne

Author

Megavolt Arsenic Implantation

into Silicon

Title

RESEARCH PROJECT

Submitted to the Department of Electrical Engineering and Computer Sciences, University of California, Berkeley, to partial satisfaction of the requirements for the degree of Master of Sciences, Plan II.

Approval for the Report and Comprehensive Examination:

Committee: Nathan Cheung, Research Adviser

Aug. 12, 1982, Date

[signature], Second Reader

Aug. 12, 1982, Date

Introduction

Advances in semiconductor technology is largely governed by our ability to control and modify materials in a well-defined manner. It is because of this control that small, fast, low power devices can be made and combined to form circuits. In contrast to diffusion processes, ion implantation excels in control, and has become the method of choice for forming dopant profiles. Another area where ion implantation can contribute to the fabrication of high quality devices is in the formation of buried dopant layers. Currently, the method used to form a buried layer begins with an implant or diffusion followed by an epitaxial growth step. A single very high energy implant can achieve a buried profile, and has advantages over the two step epitaxial technique. Specifically, ion implantation is a low temperature process with a high degree of areal uniformity not found in epitaxy processes. An ion implanted buried layer also has the advantage of being a one step process which utilizes a well developed technique.

To demonstrate the utility of high energy implantation we present in Figure 1 two implanted profiles. The dashed profile is obtained from a typical 400 keV implant of arsenic into silicon, while the solid profile is obtained by implanting at 11 MeV. The desired peak concentration of $5\times10^{16} atoms/cm^3$ requires a dose of $7.5\times10^{11} atoms/cm^2$ and $3.75\times10^{12} atoms/cm^2$ for the 400 keV and 11 MeV implants respectively. The low energy implant determines the dopant concentration in the first few thousand Angstroms of the silicon, and represents the capabilities of commercial implantation systems. The 11 MeV distribution peaks at 4.4 microns. By having energies up to 11 MeV the arsenic distribution in a silicon substrate can be controlled over a range of 4.4 microns without the use of epitaxial silicon.

Some Theoretical Considerations

The purpose of this section is to discuss the physics of MeV ion

implantation, and determine threshold energies for new mechanisms. These energies are summarized in Table 2. A detailed description of the range-energy relationships with the intervening mathematical steps necessary to produce implanted distribution curves would be out of place here. Several references are available.[1,2,3]

The fundamental energy loss equation from which the calculation begins is:

$$-dE/dx = N(S_n(E_i)+S_e(E_i)) \quad (1)$$

Here, as in all of the following equations, the variables are defined as in Table 1. The physics of the implantation process is dominated by S_n and S_e. The nuclear stopping power, S_n, represents the energy lost by an ion to screened coulomb scattering with the lattice atoms. It is this process that damages the crystal during conventional implantation, and dominates the spread in the final implanted distribution after the ions come to rest. The electronic stopping power, S_e, is the energy lost to the electrons of the target material. Since electrons are much more numerous than nuclei this term can be appreciable, but since electrons are much lighter than nuclei this term contributes much less to the spread in the final ion distribution. For ion energies less than a few hundred MeV, electrons can not cause damage.

S_n is determined using the Thomas-Fermi model of the atom. This model has produced good results for keV energies,[4] but will breakdown when nuclear interactions become important. The first threshold energy we would like to calculate is the energy necessary to cross the coulomb barrier and produce nuclear interactions.

It has long been known, particularly at Berkeley, that if one atom impinges on another at sufficient energy nuclear interactions will take place. These are strong force interactions, and require the spacing of the two nuclei to be on the order of a pion wavelength plus the sum of the two nuclear radii.[5] Empirically

this spacing has been found to be:

$$R=(A_i^{1/3}+A_t^{1/3})(1.45\times10^{-15})\ meters \tag{2}$$

This distance is small compared with the electron orbitals so a simple unscreened coulomb potential can be used to determine the energy needed to come this close in a head-on collision:

$$E_T=\frac{Z_i Z_t e^2}{4\pi\varepsilon_0 R} \tag{3}$$

These energies for B, P, and As into silicon are shown in the first column of Table 2.

The effect of crossing the coulomb barrier for semiconductor work has not been studied, but is well within the range of Berkeley's Heavy Ion Linear Accelerator (HILAC). From eqn. (2) we see that the percentage of incoming ions that would experience a nuclear interaction should not be large. The effect this percentage would have on the final ion distribution and damage distribution has not been determined.

A second consideration, is the possibility of damage done to the crystal lattice by scattered electrons. To find the energy at which this damage can occur consider two processes. The first is the scattering of an electron by an incoming atom. The second is the scattering of a lattice atom by this electron. Since the rest mass of an electron is $511keV/c^2$ this calculation should proceed in a relativistic framework. For the first interaction we have:

$$E_i+E_e=E_i'+E_e' \tag{4}$$

and

$$\vec{P}_i=\vec{P}_e'+\vec{P}_i' \tag{5}$$

For a relativistic particle we have:

$$KE=\sqrt{c^2p^2+m^2c^4}-mc^2 \tag{6}$$

where KE is the kinetic energy of the particle. The maximum energy transfer is in a head-on collision. Thus, for threshold energy calculations we get:

$$KE_e = 2m_e c^2 \frac{p_i^2 c^2}{m_e^2 c^4 + m_i^2 c^4 + 2m_e c^2 (p_i^2 c^2 + m_i^2 c^4)^{1/2}} \tag{7}$$

now since $m_i \gg m_e$ and the incoming ion is non-relativistic (i.e., for energies less than 938 A_i MeV where A_i is the nuclear mass) we get:

$$KE_e \approx 4m_e \frac{KE_i}{m_i} \tag{8}$$

Applying the same relationships to the second interaction we get:

$$KE_l = 2m_l c^2 \frac{p_e^2 c^2}{m_l^2 c^4 + m_e^2 c^4 + 2m_l c^2 (p_e^2 c^2 + m_e^2 c^4)^{1/2}} \tag{9}$$

for a head-on collision.

To determine the threshold numbers for the damage we assume that the electron must transfer 15 eV to a silicon atom, and that $m_l \gg m_e$. Fifteen eV is the energy necessary to create a Frankel defect.[12] From eqn. (9) we determine that the electron must have a kinetic energy of 165.3 keV. The second column of Table 2 contains the energies needed for B,P, and As to transfer this much energy to an electron.

This effect like the previous one has not been studied in semiconductors, but it too is within the capabilities of the HILAC. Since the highest energy electrons will be created near the surface, and the absorption of electrons follows an exponential law with distance,[17] the damage created by these electrons will be greatest near the surface. This is unlike the damage created by S_n which peaks just below R_p for high energies.

The third consideration, is the energy dependence of the electronic stopping power. This problem has been considered by Brice.[6] Three distinct regions in energy are apparent: (i) a low energy region for which the incoming ion has a velocity (v) much smaller than the orbital velocities of the electrons belonging to either the lattice or incoming atoms $\{u\text{'s}\}$, (ii) an intermediate regime where v is of the same order as some of the $\{u\text{'s}\}$, and (iii) a high energy region where v is much larger than any of the $\{u\text{'s}\}$.

As reviewed by Brice and others,[6,17] the first region is that for which the Lindhard and Firsov formulations are valid. The third region has the Bethe-Bloch stopping power, while for the second region no simple theory has been found.

From data available for ions penetrating gaseous targets, Brice has produced an empirical three parameter fit valid in all three regions. The expression is somewhat complicated, and is not reproduced here, rather plots of the electronic stopping power for the standard cases are shown in Figures 2a,2b, and 2c. These plots were generated using the Brice formula with the parameters interpolated from the Tables given in reference [1].

The plots of S_e show that a maximun in the electronic stopping is obtained with S_e falling off for higher energies. The major consequence of this effect should be an enhanced increase of R_p as a function of energy once we cross the maximum in the electronic stopping power. The energies at which this will occur for the standard case are given in column 3 of Table 2. Experimental measurements of this effect for semiconductors has not been reported, but recently we have exposed silicon to 4 MeV boron atoms in the hopes of measuring the increased range. Details of the finding will be reported in future work.

There may exist other high energy effects, but the amount of data above 1 MeV for semiconductor work is very limited.

Experimental Conditions

The implantations were carried out using the facilities of the Lawrence Berkeley Laboratory. Eleven MeV arsenic beams were obtained from a dynamatron with a 2.2 megavolt terminal. The ion source is a conducting crystal of gallium arsenide from which arsenic ions in the 5+ charge state were sputtered and extracted into the accelerator column. The beam current used was $1.3\pm.3\mu amps$ with a $1.0\pm.2\ cm^2$ spot size. A dose of $1.9\times10^{15} atoms/cm^2$ was

deposited for all the samples. The specimens can be either water-cooled to a nominal temperature of 300° K or liquid nitrogen cooled to 77° K. Annealing was carried out in a flowing nitrogen ambient at 545° C for 16 hours followed by a 965° C cycle for 15 minutes. The times were chosen to allow for solid-phase regrowth over 5 microns of silicon, and to achieve electrical activation.[7]

A criterion which is of central importance is whether the implanted silicon can be returned to a device quality state after implantation. This means that pn junctions must be located in dislocation free silicon. The carrier mobility and minority carrier lifetime should also be maximized.[12] To characterize the damage created by the implantation, Rutherford backscattering spectrometry (RBS) and cross-sectional transmission electron microscopy (XTEM) were used. For the RBS measurements 2 MeV helium nuclei were channeled along the <100> axis and their backscattered yields recorded. Table 3 summarizes the results of the RBS measurements. In this Table, χ_{min} is the ratio of backscattering yields for the implanted sample divided by the yield for a randomly aligned crystal. The yields used are those from the helium ions that are scattered from silicon atoms just below the crystal's surface. The backscattered spectra also contain information about the silicon lattice from the upper one micron. With the exception of the unannealed LN-cooled sample the spectra obtained from the implanted and unimplanted silicon show insignificant differences over this first micron. Specifically, the room temperature implant shows crystalline characteristics before furnace annealing down to one micron while the LN-cooled sample is amorphous in this region.

To obtain information about defect densities over the full range of the implant XTEM was used.[8] Figures 3a and 3b contain the XTEM micrographs of the as-implanted silicon for both LN-cooled and water-cooled substrates. The dark bands represent the amorphous regions in these bright-field micrographs. It is

evident that the widths of these amorphous bands depend strongly on the substrate temperature during implantation. Comparison between the water-cooled and LN-cooled specimens shows that dynamic annealing during the $300^{\circ}K$ implantation is significant, with in situ recrystallization taking place mainly in the upper portion of the amorphous band.

Since the creation of amorphous silicon is related to lattice displacement, the energy per unit distance (eV/A) deposited into nuclear stopping, Q_n, has been generated from the tables of Brice.[1] Q_n is the integral over the range of the implanted damage of the energy deposited into the motion of silicon atoms. This integral includes contributions from the damage cascade as well as the energy deposited by the incoming ion S_n. From Figure 4, it is observed that the boundaries of the amorphous band occur at approximately the same energy density for the room temperature implant. The LN-cooled sample shows a slightly lower threshold toward the surface. If a threshold energy, Q_T, is defined as the value of Q_n at the amorphous interface, then the Q_T value is determined to be $24 \pm 1 eV/A$ for the water-cooled sample, and $11 \pm 3 eV/A$ for the LN cooled sample. These Q_T values correspond to energy densities of $4.56 \times 10^{21} keV/cm^3$ and $2.1 \times 10^{21} keV/cm^3$. The energy density found for the LN-cooled sample is higher than the energy density required for low energy ion implantations.[9]

The micrographs in Figure 3 both show a more abrupt amorphous-crystalline interface at the lower boundary than the upper boundary. This observation can be explained by the more gradual change of Q_n at the upper interface as compared with the rapid change of Q_n at the lower interface. Physically, the energy carried by the recoil silicon atoms will influence the interface sharpness. Near the lower interface most of the recoil atoms will carry small kinetic energies and have negligible straggling in their range.

The sharpness of the interfaces has also been observed (Figure 3) to be

dependent on the implantation temperature. The movement of interstitials or vacancies is required for recrystallization, and since the diffusion length of vacancies and interstitials increases with temperature, the interface is less abrupt for the water-cooled case. For LN-cooling in situ annealing is not as important.

The XTEM micrographs of the annealed specimens are shown in Figure 5. Regrowth features indicate that solid-phase recrystallization proceeds from both upper and lower interfaces. Crystalline quality of regrown layers from the lower interface ranges from dislocation free crystal for the LN-cooled specimen to low dislocation densities for the water-cooled specimen. In contrast, dense dislocation networks are observed in the regrown layers originating from the upper regrowth interface for both types of specimens. The regrowth fronts meet approximately at the mid-distance between the regrowth interfaces, indicating that the regrowth rates are almost the same for both regrowth fronts. In addition to the dislocations in the middle of the implanted region, a large concentration of stacking fault tetrahedra (SFT) and small dislocation loops were present in the surface region, extending down to a depth of 1500 Angstroms. The SFT's indicate the presence of vacancies at the surface.[10]

In summary, the discrete layers of secondary defects formed during the anneal are similar to those observed for lower energy implantations.[11,12] The narrow band of defects (interstitial type) at the lower regrowth interface for the LN-cooled sample, and just below the lower interface for the water-cooled sample has also been observed previously with implantation in the 100 keV region. This band is visible only after annealing, and its formation mechanism is still under investigation.

Device Considerations

High energy implantation has made possible some novel and perhaps

important device structures.[13,14,15,16] Save for [16], these structures have been fabricated using beams with energies between 1 and 5 MeV; in our work the energy has been extended to 11 MeV. By increasing the energy it is possible to obtain highly doped buried layers while keeping the surface concentration low. In this way, not only conventional device structures benefit, but three dimensional usage of the silicon may also be possible.

For device applications Figure 5 (b) is of particular interest because the upper two microns of the substrate contains defects only at the surface, and is recrystallized by in situ annealing during the implantation process. The perfection of this region is further confirmed by higher resolution weak-beam TEM micrographs which indicate the absence of secondary defects. It is also interesting to note from Figure 3 (a) that if the upper 1 micron of silicon is removed before annealing then the regrown material would start from the bottom interface only, and may regrow cleanly.

In summary, residual damage exists for both room temperature and LN temperature implantation conditions. The effect of this damage on device performance and yield can only be determined in an active device environment where leakage currents and noise performance can be measured. It should be pointed out that all of the implants performed for this study have been at a high dosage. The residual damage for low dose or light ions has yet to be determined.

A spreading resistance curve for an implant is shown in Figure 6. The error in concentration (y-axis) can be as large as a factor of two, while the depth (x-axis) is known to 4%. The peak concentration is below the predicted value of $2 \times 10^{19} atoms/cm^3$. This could possibly result from bad activation or poor charge integration of the implanted dose. The peak at 4.4 microns agrees with LSS predictions, and with an independent secondary ion mass spectrometry measurement. Two background concentrations that are interesting for device

purposes are also depicted. For a typical p-type background concentration of $5\times10^{16}/cm^3$ the implanted active arsenic would produce an n-type region extending from 3 to 5 microns beneath the surface.

An application for such a distribution is shown in Figure 7. Here buried interconnects are fabricated by first diffusing a phosphorus well, and then implanting a buried channel. The channel can be defined using a mask composed of gold, tungsten, or some other heavy element. Tungsten, being a refractory metal with good adhesion to silicon dioxide, is preferable. Successful masking for 11 MeV arsenic ions requires approximately 2.5 microns of either gold or tungsten.

Resistance values for different length interconnects are shown in Figure 8. This technique may offer another layer of independent interconnection for increasingly complex NMOS circuits. The obtained sheet resistance of 50 $\Omega/square$ is sufficient for short paths, and with increased dopant concentration poly-like resistances can be obtained.

In conclusion, a high energy implant process has been demonstrated and buried interconnects have been fabricated. Research in this area is ongoing, with other applications under active study.

The author would like to thank Prof. N.W. Cheung for much support and discussion, D.K. Sadana for the XTEM micrographs, and M. Strathman, C. Drowley, and Prof. J. Washburn for discussions and aid. It is also a pleasure to acknowledge R. Stevenson, J. Gavin, R. Thatcher, and the other members of the Lawrence Berkeley Laboratory Heavy Ion Linear Accelerator staff for allowing us to use their facility. This research was partially supported through AFOSR F49620-79-C-0178 and NSF contract ECS-8105972.

REFERENCES

1. D.K. Brice, *Ion Implantation Range and Energy Deposition Distributions Volume 1* (Plenum, New York, 1975).

2. J.W. Mayer, L. Eriksson, and J.A. Davies, *Ion Implantation in Semiconductors Silicon and Germanium* (Academic Press, New York, 1970).

3. J.F. Gibbons, Proc. IEEE, vol. 33, (1963) p. 295.

4. L.A. Christel, J.F. Gibbons, and S. Mylroie, J. Appl. Phys. **51**, 6176 (1980).

5. E. Segre, *Nuclei and Particles* (Benjamin/Cummings, Reading, 1977) p. 597.

6. D.K. Brice, Phys. Rev. A **6**, 1791 (1972).

7. S.S. Lau, and W. F. van der Weg, in *Thin Films Interdiffusion & Reactions*, (eds. J.M. Poate, K.N. Tu, and J.W. Mayer) (Wiley-Interscience, New York) (1978) 433.

8. P.F. Byrne, N.W. Cheung, and D.K. Sadana, To be published in Applied Physics Letters.

9. L.A. Christel, J.F. Gibbons, and T.W. Sigmon, Appl. Phys. Lett. **52**, 7143 (1981).

10. J. Silcox, and R.B. Hirsch, Phil. Maj. (1958) pg. 72.

11. D.K. Sadana, M. Strathman, J. Washburn, C.W. Magee, M. Maenpaa, and G.R. Booker, Appl. Phys. Lett. **37**, 615 (1980).

12. J.F. Gibbons, Proc. IEEE, vol. 60, (1972) p. 1052.

13. J.F. Ziegler, B.L. Crowder, and W.J. Kleinfelder, IBM J. Res. Develop., Nov., (1971) 452.

14. D.P. Lecrosnier, and G.P. Pelous, IEEE Trans. Electron Devices, ED-21, (1974) 113.

15. M. Doken, T. Unagami, K. Sakuma, and K. Kajiyama, IEDM, (1981) 586.

16. P.F. Byrne, N.W. Cheung, and D.K. Sadana, presented at the *International Conference on Metallurgical Coatings and Process Technology*, (1982) To be published in Thin Solid Films.

17. L.T. Chadderton, *Radiation Damage in Crystals* (Meuthuen, London, 1965)

Table 1

Definition of Variables

Variable	Definition
A	Nuclear Mass (amus)
c	Speed of Light
e	Charge on an Electron
E	Energy
E_T	Threshold Energy
ε_o	Permittivity of Free Space
KE	Kinetic Energy
m	Mass
N	Average Number of Ions at x
P	Momentum
Q_n	Energy Deposited into Nuclear Stopping
Q_T	Threshold Energy Deposited
R	Coulomb Barrier Spacing
R_p	Projected Range
ΔR_p	Standard Deviation of Projected Ion Distribution
S_e	Electronic Stopping Power
S_n	Nuclear Stopping Power
x	Distance Along Ion's Path
Z	Atomic Number

Subscripts and Superscripts

Symbol	Meaning
i	Ion
l	Lattice Atom
e	Electron
primed	After Collision
unprimed	Before Collision

Table 2

Threshold Energies for Standard Ions implanted into silicon (MeV)

Ion	Coulomb Barrier	Electronic Damage	Electronic Stopping Peak
Boron	10.5	835.	2.5
Phosphorus	33.7	2350.	14.0
Arsenic	63.2	5700.	80.0

Table 3

Substrate Cooling	χ_{min}	Furnace Anneal
LN	100%	No
LN	5%	Yes
Water	5%	No
Water	5%	Yes
Unimplanted (100) Si	4%	-

FIGURE CAPTIONS

Figure 1. Arsenic concentration versus depth for 400 keV (dashed line) and 11 MeV (full line) implantations. A Gaussian approximation was used in this calculation.

Figure 2. Electronic stopping power S_e as a function of energy for boron into silicon (a), phosphorus into silicon (b), and arsenic into silicon (c).

Figure 3. XTEM micrograph of implanted silicon before furnace anneal. (a) and (b) are the LN-cooled and water-cooled samples respectively. Sketches of salient features are presented on the right. The dashed line in (b) drawn from information contained in Figure 5(b).

Figure 4. Energy deposition curve from Brice with the positions for the amorphous interfaces. The closed circles are for the LN-cooled sample while the open circles are for the water-cooled sample.

Figure 5. XTEM micrograph of implanted silicon after furnace anneal. (a) and (b) are the LN-cooled and water-cooled samples respectively. Sketches of salient features are presented on the right.

Figure 6. Spreading resistance measurement of active arsenic concentration versus depth.

Figure 7. Cross section view of buried interconnect.

Figure 8. Resistance versus length for a set of interconnects.

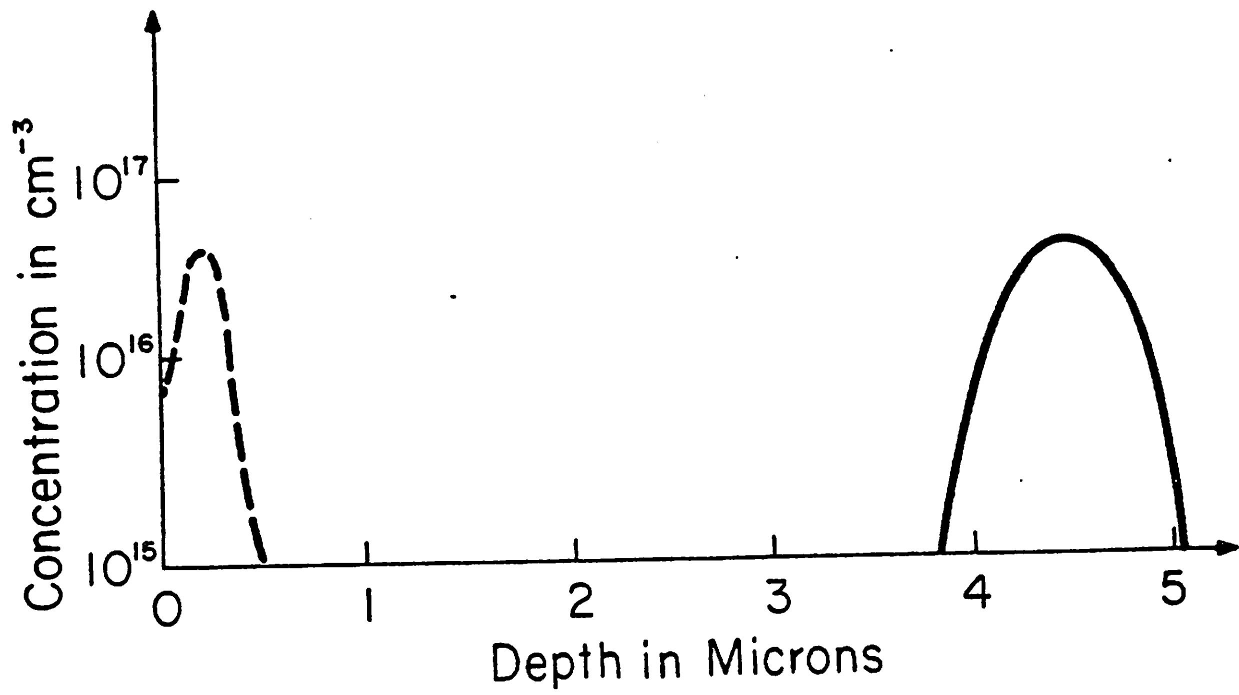

Figure 1

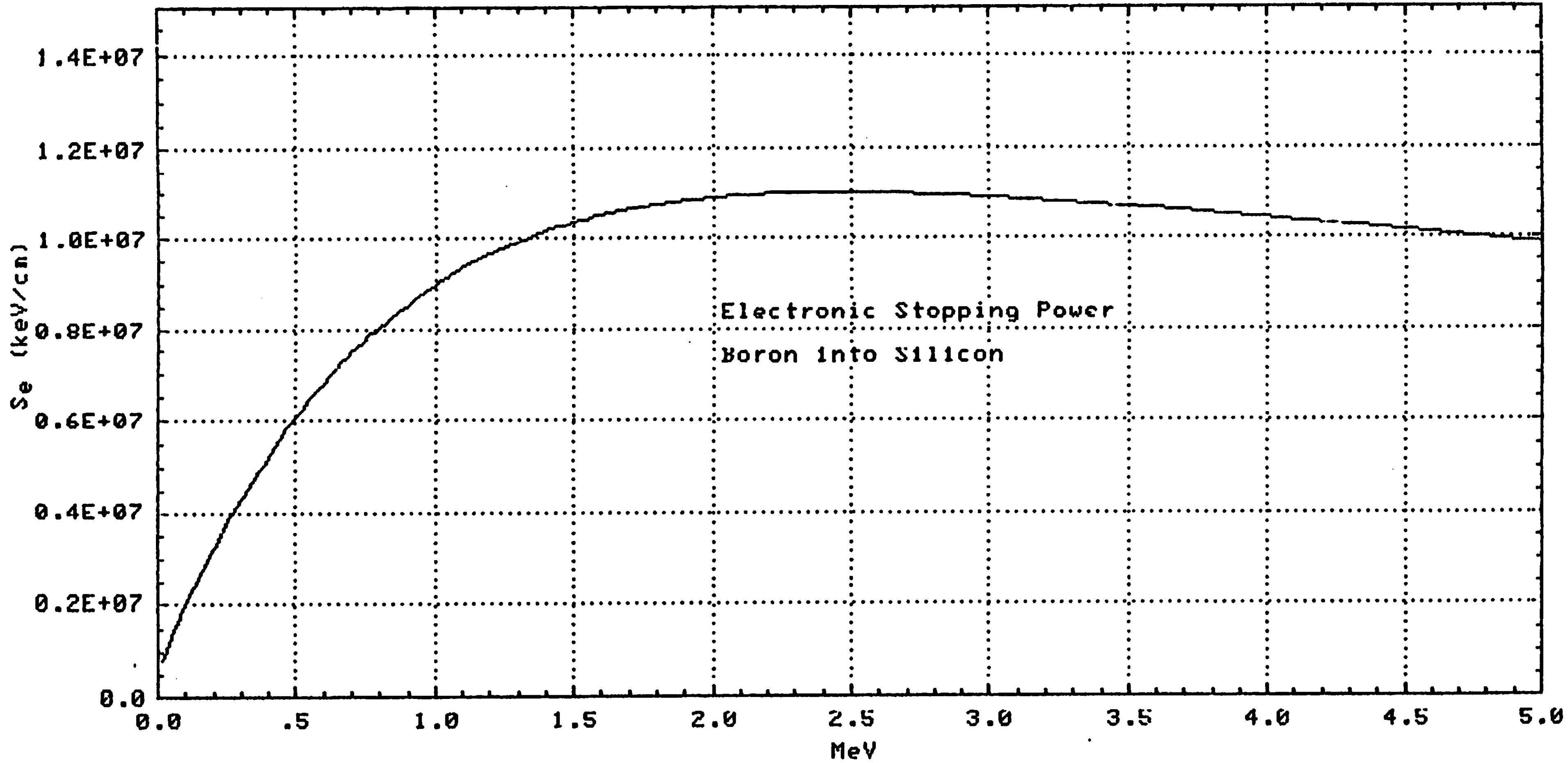

Figure 2 (a)

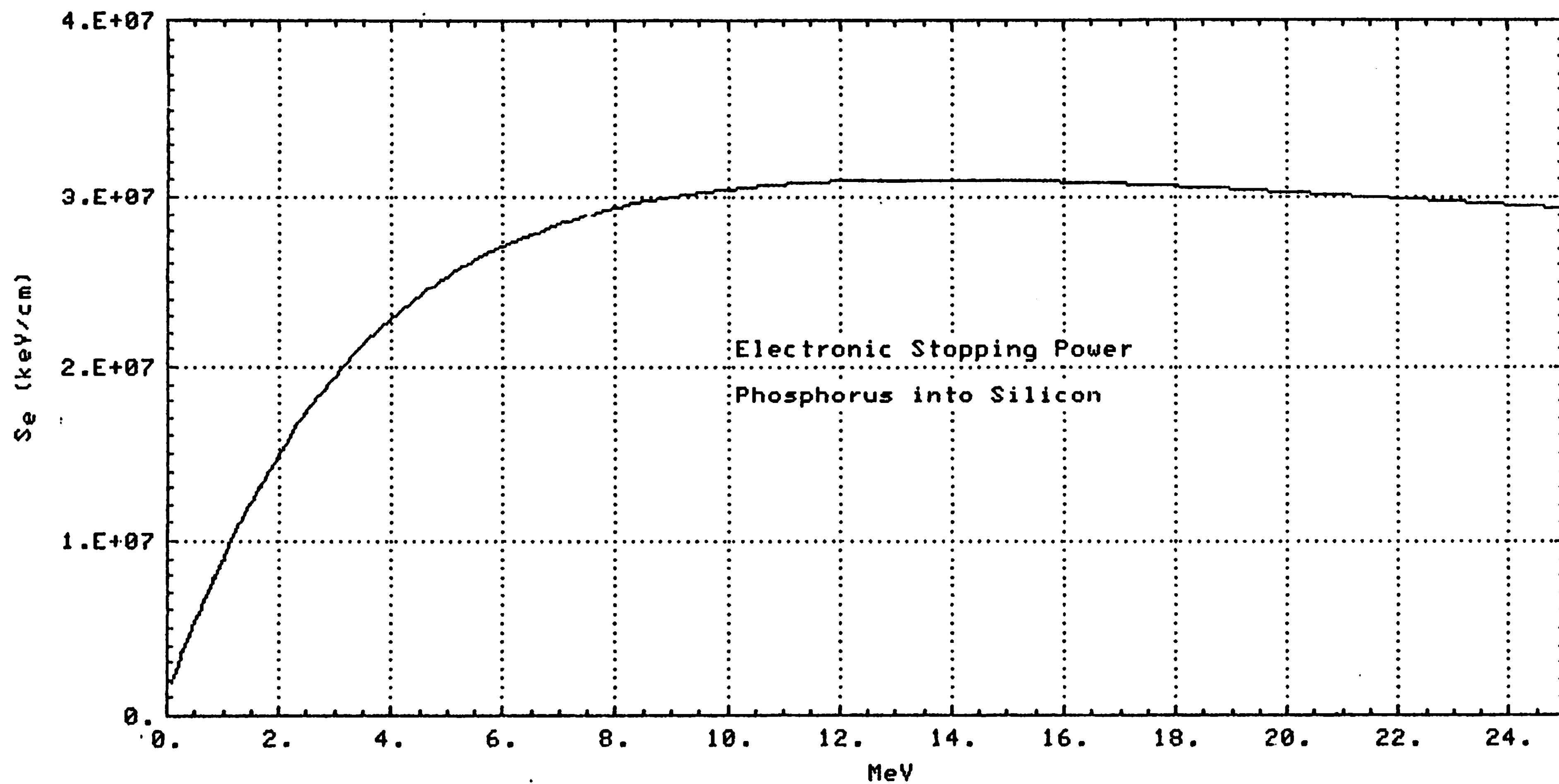

Figure 2 (b)

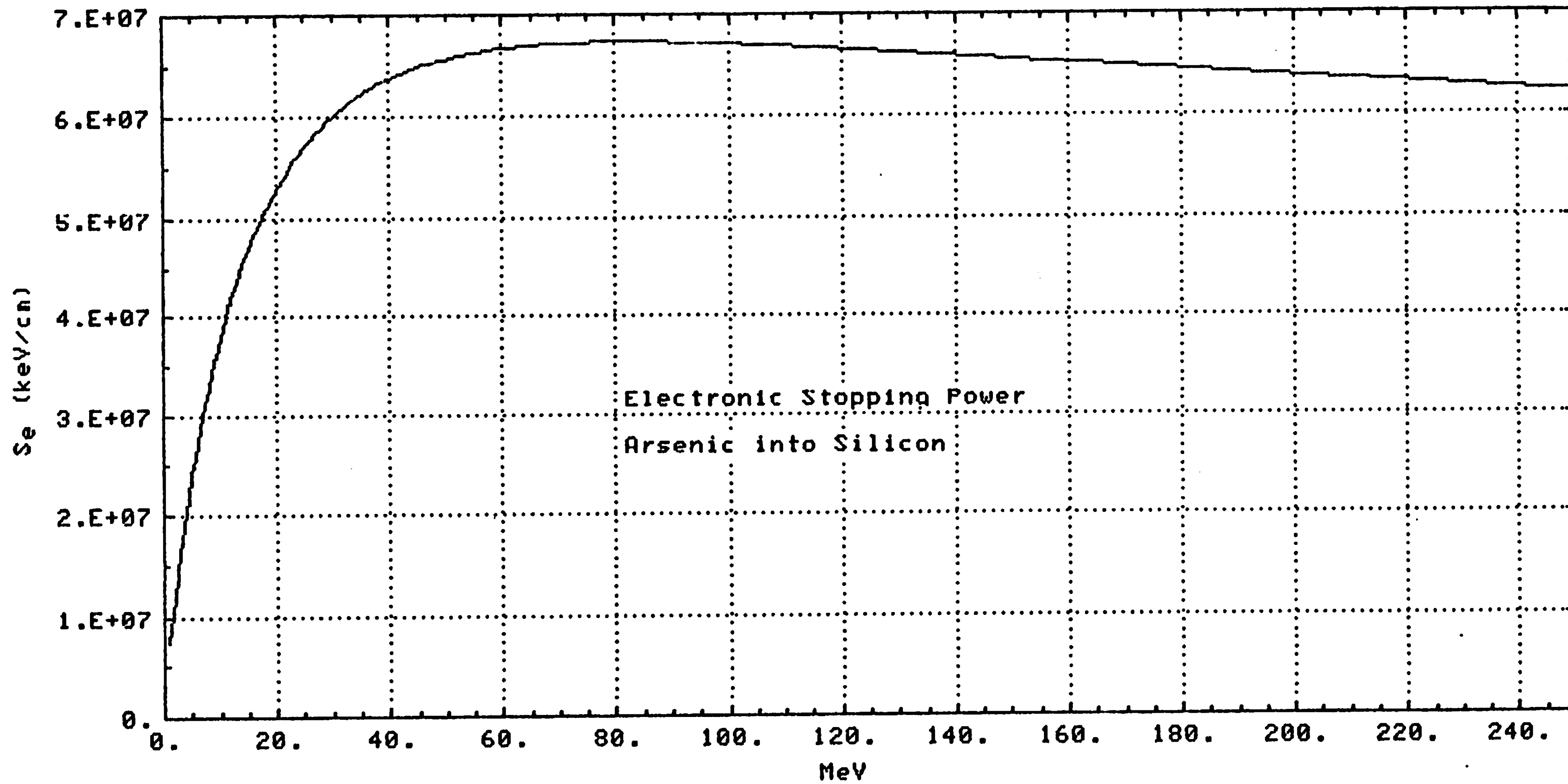

Figure 2 (c)

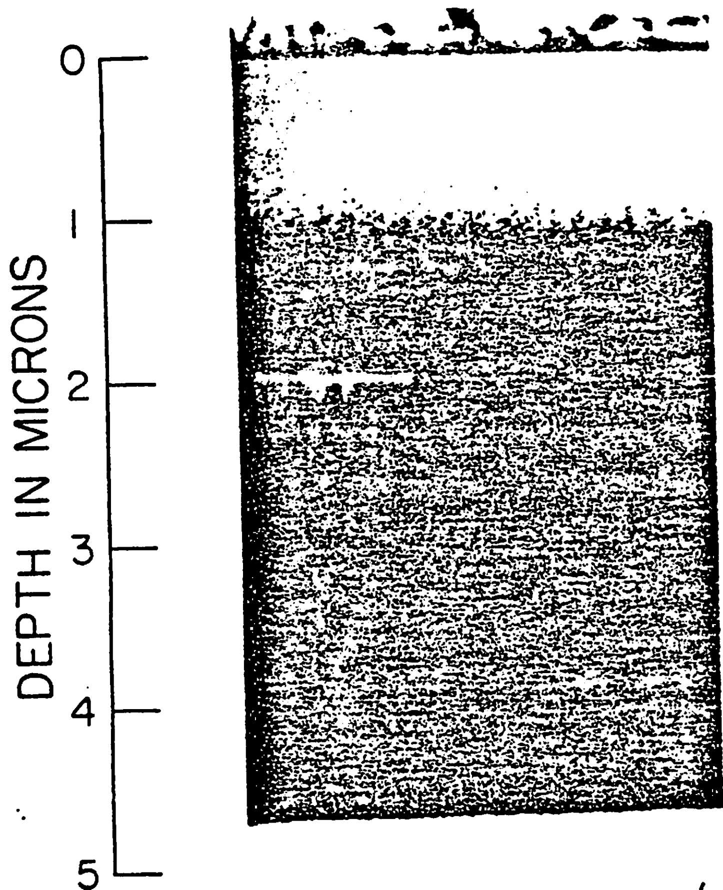

Amorphous & Crystalline Mixture

Amorphous

(a)

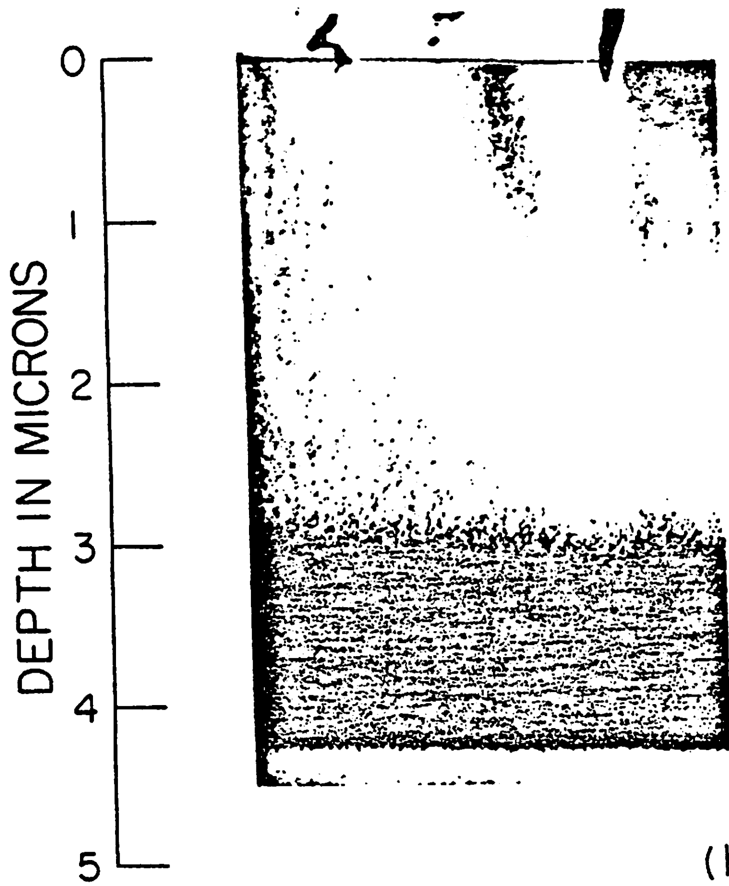

Crystalline

Amorphous & Crystalline Mixture

Amorphous

(b)

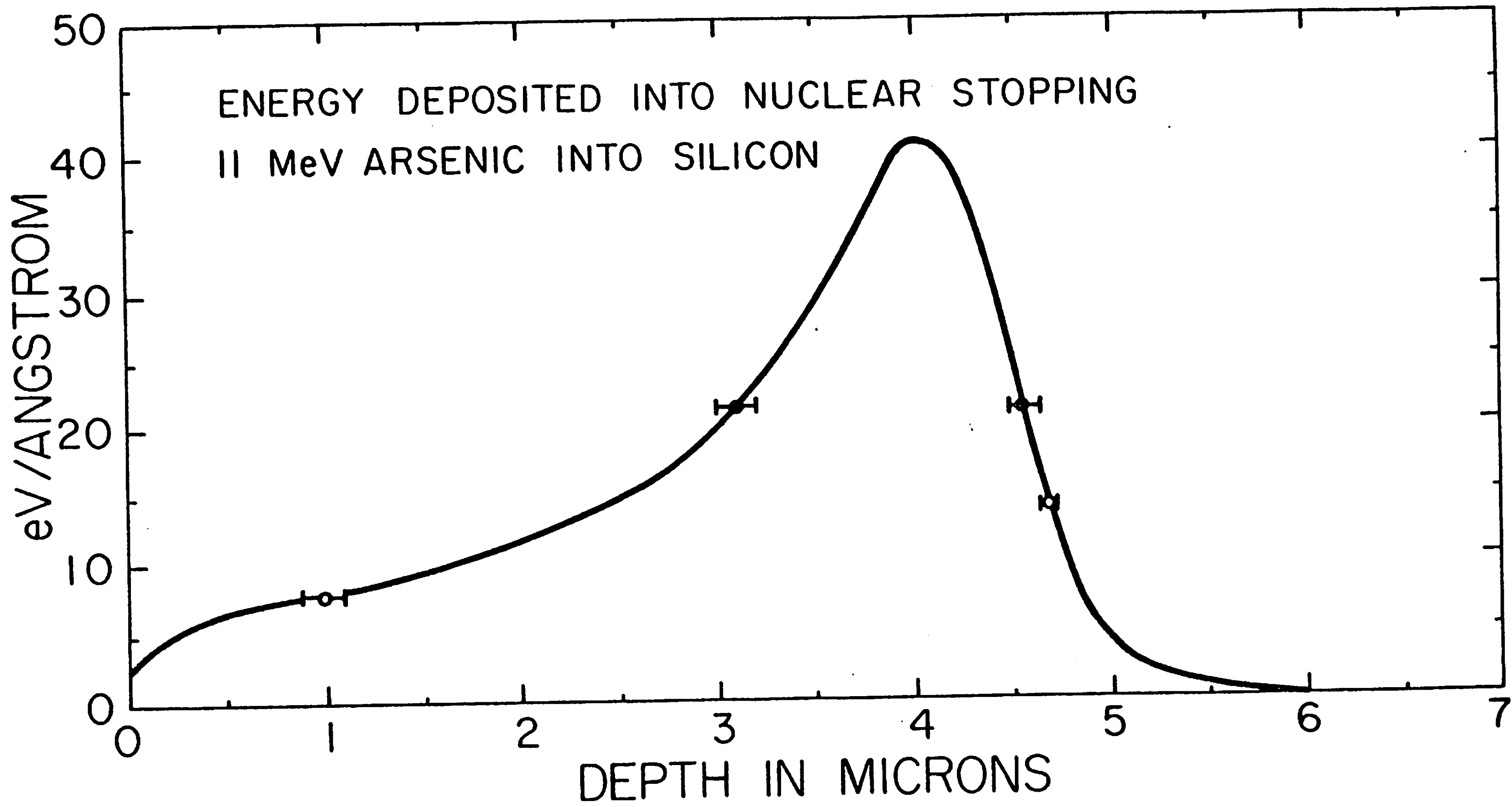

Figure 4

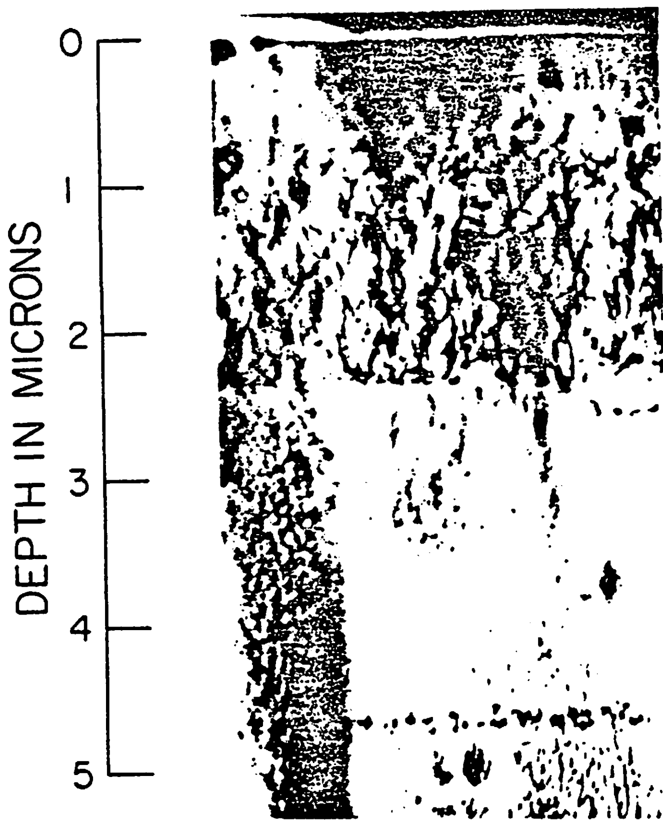

(a)

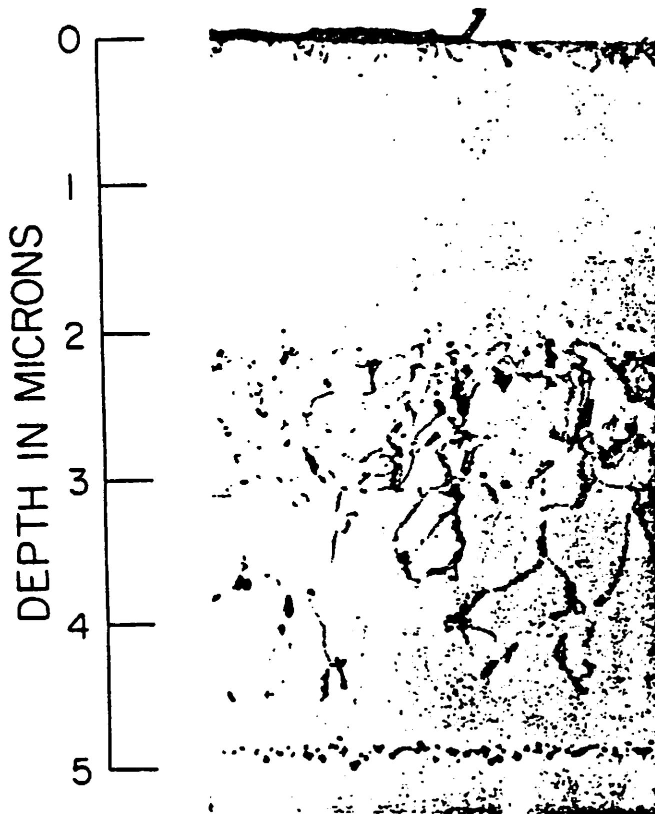

(b)

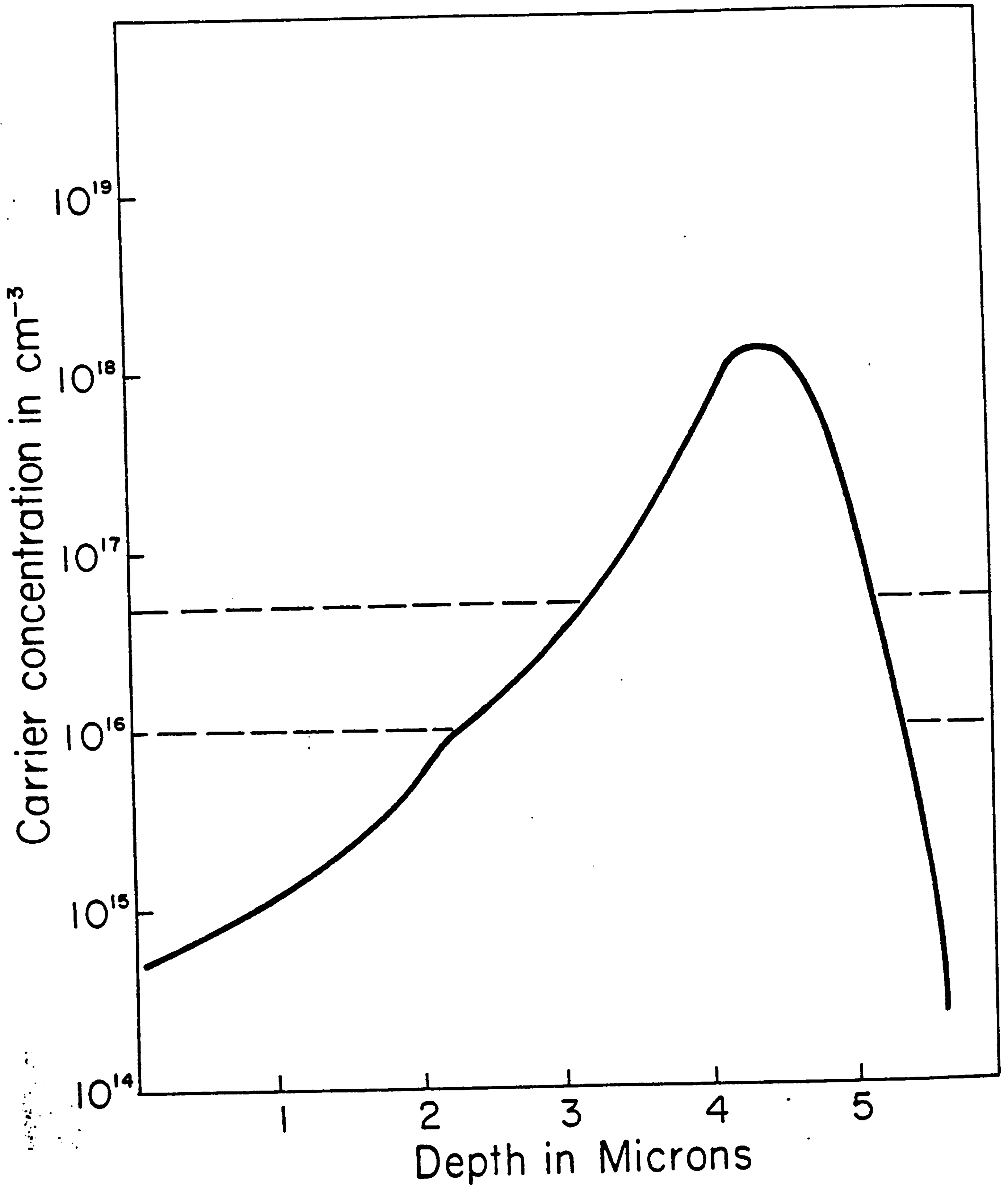

Figure 6

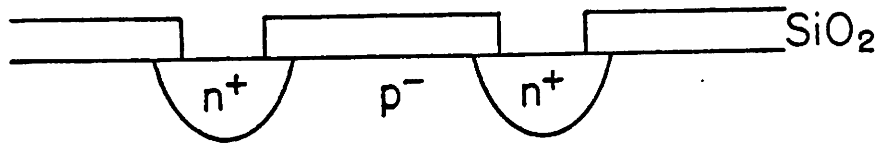

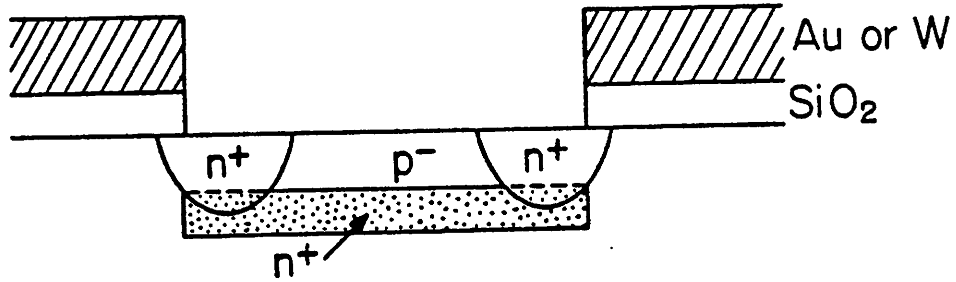

Figure 7

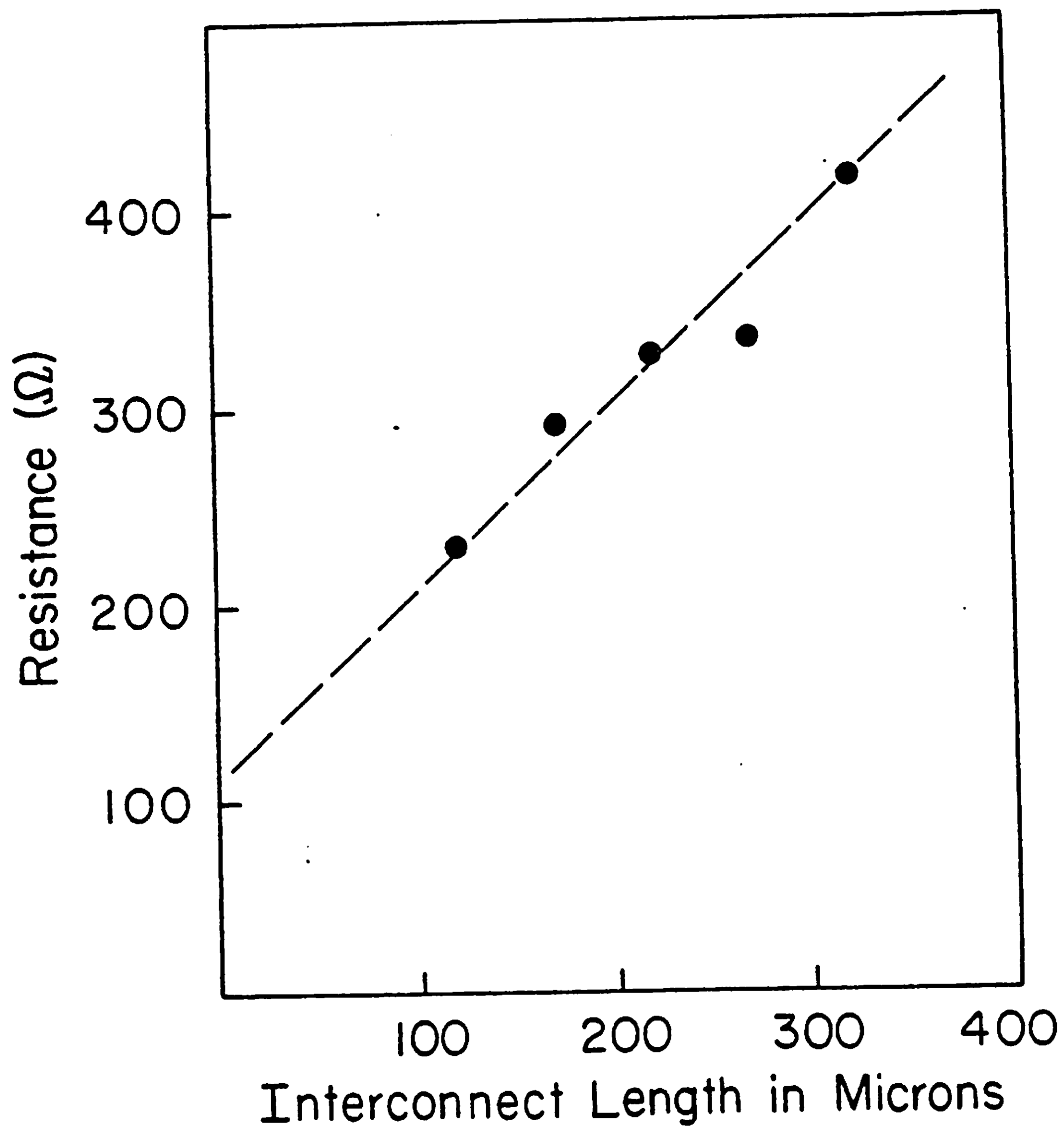

Figure 8